

1 **Estimating the impact of a major hurricane on**
2 **transport processes**

3 Thomas Dobbelaere, Emmanuel Hanert

4 February 16, 2021

5 **Abstract**

6 In most hydrodynamic model studies, currents and waves are simu-
7 lated separately. This is especially true for the simulation of passive
8 drifters, whose trajectories are often computed based solely on cur-
9 rents. Although this simplification holds for most situations, as the
10 force exerted by waves on currents can be neglected in fair weather
11 conditions, it may lead to significant errors in storm conditions, during
12 which local currents are strongly influenced by wind-generated waves.
13 In this study, current-wave interactions in heavy-wind conditions are
14 studied by coupling the unstructured-mesh hydrodynamic model SLIM
15 with the wave model SWAN in the Florida Reef Tract during Hurricane
16 Irma (Sep. 2017). This coupled model successfully reproduced both
17 the observed wave behavior and storm surge during the hurricane.
18 The modeled currents were then used to simulate the trajectories of
19 passive drifters during the passage of the hurricane. Our results show
20 that taking wave force into account induces variations of up 1 m/s in
21 modelled currents on the continental shelf break as well as in the vicin-
22 ity of reefs and islands. Wave-current interactions can therefore deflect
23 the trajectories of drifting material by up to 10 km during heavy-wind
24 events. These results strongly advocate for the inclusion of wave forces
25 while studying transport processes (sediments, pollutants, larvae, etc.)
26 under storm conditions

27 **1 Introduction**

28 Wave-current interactions in coastal areas are of great importance for coastal
29 engineering as they play a key role in sediment transport, morphological
30 evolution and pollutant mixing (Bever and MacWilliams, 2013; Li and Johns,
31 1998). However, these interactions are highly nonlinear and can vary sig-
32 nificantly in space and time (Wu et al., 2011). Wave-induced currents are
33 generated by wave radiation gradients (Longuet-Higgins, 1970), affecting
34 water levels near shorelines and wave breaking points (Longuet-Higgins
35 and Stewart, 1964), while changes in water levels and currents, in turn,
36 affect the motion and evolution of waves (Sikirić et al., 2013). Coupled
37 wave-current models are therefore required to capture these complex inter-
38 actions. As coastal oceans are characterized by local complex geometries
39 with islands, inlets and estuaries, unstructured (usually two-dimensional)
40 models are preferred as structured grid models show limitations in resolving
41 topologically controlled nearshore processes (Wu et al., 2011; Chen et al.,
42 2007). The effect of wave-interactions becomes even more significant in
43 the case of hurricanes, that generate large wind-waves and disturb ocean
44 conditions (Liu et al., 2020) by causing coastal upwellings on continental
45 shelves (Smith, 1982) and inducing strong currents, waves and storm surges
46 in nearshore and coastal regions (Dietrich et al., 2010; Weisberg and Zheng,
47 2006). South Florida and the Gulf of Mexico are particularly vulnerable to
48 hurricanes (Malmstadt et al., 2009) and modelling studies predict tropical
49 cyclones to increase both in frequency and intensity in this region (Mar-
50 sooli et al., 2019; Knutson et al., 2010). Being able to accurately model
51 wave-current interactions in this area becomes thus critical.

52 Individual-based modelling of particulates has been extensively used to
53 study the transport of drifting materials such as pollutants, sediments or
54 larvae (Garcia-Pineda et al., 2020; Liubartseva et al., 2018; Figueiredo et al.,
55 2013; Frys et al., 2020). Although some of these studies take the impact
56 of waves into account by adding Stokes drift velocity, *i.e.* the net drift of a
57 floating particle in the direction of the wave propagation (Van Den Bremer
58 and Breivik, 2018), to the Eulerian currents, they usually neglect the wave-
59 induced currents. Such practice is reasonable in the case of fair weather,
60 when wave-induced forces exerted on currents are relatively smaller, but
61 might lead to significant inaccuracies during storm conditions. To assess

62 the importance of wave-current interactions during a tropical cyclone, we
63 investigated the transport of drifting particulates on the Florida shelf during
64 Hurricane Irma, one of the strongest and costliest tropical cyclones on
65 records in the Atlantic Basin (Chen et al., 2007), that made landfall in Florida
66 in September 2017.

67 In this study, we developed an unstructured coupled wave-current model of
68 South Florida to simulate the ocean circulation during hurricane Irma. Both
69 modelled currents and waves were validated against field measurements
70 and were then used to simulate the transport of drifting particulates in the
71 Florida Keys and the Florida inner shelf during the storm. Model outputs
72 were then compared with uncoupled simulation results in order to assess
73 the impact of wave-induced forces and Stokes drift on the modelled currents
74 and transports.

75 **2 Methods**

76 **2.1 Study area and data**

77 Large-scale ocean circulation around South Florida is dominated by the
78 Florida Current (FC), which originates from the Loop Currents (LC) where it
79 enters the Florida Straits from the Gulf of Mexico, and, downstream, forms
80 the Gulf Stream. The FC is a major western boundary current character-
81 ized by spatial variability and meandering, associated with the presence
82 of cyclonic eddies between the core of the current and the complex reef
83 topography of the Florida Reef Tract (FRT) (Frys et al., 2020; Lee et al.,
84 1995; Kourafalou and Kang, 2012). The northern half of these reefs are
85 made of early Holocene reef frameworks and indurated sand ridges while
86 the southern part (the Florida Keys) is composed of a chain of limestone is-
87 lands, fossilized remnants of ancient coral reefs and sand bars (Hoffmeister
88 and Multer, 1968; Shinn, 1988; Lidz and Shinn, 1991). The variability of the
89 FC extends over a large range of spatial and temporal scales, with periods
90 of 30-70 days in the Lower Keys (Lee et al., 1995) and shorter periods of
91 2-21 days in the Upper Keys (Lee and Mayer, 1977), and exhibits significant
92 seasonal and interannual cycles (Johns and Schott, 1987; Lee and Williams,
93 1988; Schott et al., 1988). Circulation on the West Florida Shelf (WFS) on

94 the other hand is forced by local winds and tidal fluctuations (Lee and Smith,
95 2002; Liu and Weisberg, 2012).

96 Field observations were used to validate our model outputs. Modelled sea
97 surface elevation was validated against tide gauge measurements from
98 the National Oceanic and Atmospheric Administrations (NOAA) Tides and
99 Currents dataset. These measurements were taken at four locations: two
100 in the Florida Keys (Key West and Vaca Key); one on the eastern coast
101 of Florida (Key West); and one on the western coast (Naples). Currents
102 were validated against ADCP measurements from the University of South
103 Florida's College of Marine Science's (USF/CMS) Coastal Ocean Monitoring
104 and Prediction System (COMPS) for the WFS (Weisberg et al., 2009). More
105 specifically, we used measurements from moorings C10, C12 and C13,
106 respectively located at the 25, 50, and 50 m isobaths of the WFS (Liu
107 et al., 2020). Finally, validation of modelled wave parameters was performed
108 against four buoy measurements from NOAA's National Data Buoy Center
109 (NDBC): two on Florida's Eastern shelf and two on the WFS. The locations
110 of all measurement stations are shown on Fig. 1

111 **2.2 Wind and atmospheric pressure for Hurricane Irma**

112 Irma made landfall in Florida on 10 September 2017 as a category 3 storm,
113 first at Cudjoe Key (Florida Keys) and later on Marco Island, south to Naples
114 (see Fig. 1). It then weakened to a category 2 storm as it moved further
115 inland (Pinelli et al., 2018). The storm caused damages to up to 75% of
116 the buildings at his landfall point in the Florida Keys, making it one of the
117 strongest and costliest hurricanes on record in the Atlantic basin (Xian
118 et al., 2018; Zhang et al., 2019). The strongest reported wind speed was
119 50 m/s on Marco Island while the highest recorded storm surge was 2.3
120 m, although larger wind speed likely occurred in the Florida Keys (Pinelli
121 et al., 2018) In order to reproduce the wind profile of Irma in our model,
122 high-resolution H*Wind (Powell et al., 1998) wind fields were used. As
123 these data represent 1-min averaged wind speeds, we multiplied them by
124 a factor 0.93 to obtain 10-min averaged wind speeds (Harper et al., 2010),
125 more consistent with the time step of our model. Furthermore, H*Wind
126 wind profiles did not cover the whole model extent during the hurricane and

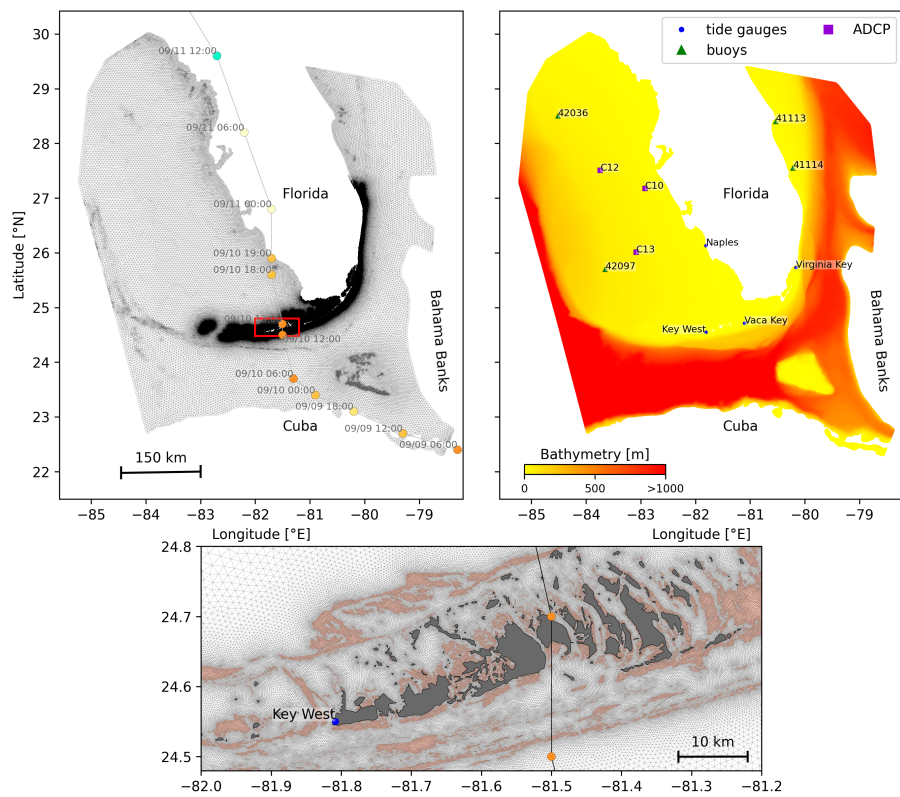


Fig. 1: Upper left: Mesh of the computational domain with the trajectory of Irma, category of the hurricane is given by the Saffir-Simpson color scale. Upper right: Bathymetry of the domain with the location of stations used for the validation of the model outputs. Lower center: Close up view of the 100m mesh resolution near reefs and islands; islands are highlighted in dark grey and coral reefs in coral

127 were thus blended within coarser wind field extracted from ECMWF ERA-5
 128 datasets. Pressure fields of Irma were also constructed using ERA-5 data.
 129 However, the coarse resolution of the data set caused the depression at the
 130 center of the hurricane to get smoothed out, leading to an underestimation
 131 of the pressure gradient in our model (see eq. 1). To better capture the
 132 central depression of Irma, we built a hybrid pressure field using the position
 133 and the minimal pressure of the core of the hurricane based on its track
 134 in the HURDAT 2 database (Landsea and Franklin, 2013). Based on this
 135 information, the hybrid pressure field was constructed by combining an
 136 idealized Holland pressure profile (Lin and Chavas, 2012) within the radius
 137 of maximum wind speed of Irma (Knaff et al., 2018) with ERA-5 pressure
 138 field. The transition between from the Holland profile to ECMWF data outside
 139 the radius of maximum wind speed data was performed using a smooth step
 140 function.

141 **2.3 Hydrodynamic model**

142 Ocean currents generated during hurricane Irma around South Florida
 143 were modelled using the unstructured-mesh depth-integrated coast ocean
 144 model SLIM¹. The model mesh covers an area similar to the model extent
 145 of Dobbelaere et al. (2020b), that includes the FRT but also the Florida
 146 Strait and part of the Gulf of Mexico (Figure 1). However, this area has
 147 been slightly extended northeastward and westward in order to include
 148 the location of buoys for wave outputs validation. Furthermore, in order to
 149 withstand potential cell drying due to storm conditions in this study, we used
 150 the conservative mode of SLIM with wetting-drying, whose equations write:

$$\begin{aligned}
 \frac{\partial H}{\partial t} + \nabla \cdot (\mathbf{U}) &= 0 \\
 \frac{\partial \mathbf{U}}{\partial t} + \nabla \cdot \left(\frac{\mathbf{U}\mathbf{U}}{H} \right) &= -f \mathbf{e}_z \times \mathbf{U} + \alpha g H \nabla(H - h) - \frac{1}{\rho} \nabla p_{\text{atm}} + \frac{1}{\rho} \boldsymbol{\tau}_s \quad (1) \\
 &\quad + \nabla \cdot (\nu \nabla \mathbf{U}) - \frac{C_b}{H^2} |\mathbf{U}| \mathbf{U} + \gamma (\mathbf{U}_* - \mathbf{U})
 \end{aligned}$$

151 where H is the water column height and \mathbf{U} is the depth-averaged transport;
 152 f is the Coriolis coefficient; g is the gravitational acceleration; h is the

¹<https://www.slim-ocean.be>

153 bathymetry; α is a coefficient stating whether the mesh element is wet
 154 ($\alpha = 1$) or dry ($\alpha = 0$); ν is the viscosity; C_b is the bottom drag coefficient;
 155 ∇p_{atm} is the atmospheric pressure gradient; τ_s is the surface stress due
 156 to wind; and γ is a relaxation coefficient towards a reference transport \mathbf{U}_* .
 157 As in Frys et al. (2020) and Dobbelaere et al. (2020b), SLIM currents were
 158 relaxed towards HYCOM (Chassignet et al., 2007) in regions where the water
 159 depth exceeds a given threshold. At very high wind speeds, the white cap is
 160 blown off the crest of the waves, which generates a layer of droplets that acts
 161 as a slip layer for the winds at the ocean-atmosphere interface (Holthuijsen
 162 et al., 2012). This causes a saturation of the wind drag coefficient for strong
 163 winds (Donelan et al., 2004; Powell et al., 2003). To account for the impact
 164 of this saturation on the surface wind stress in our model, we implemented
 165 the wind drag parameterization of Moon et al. (2007).
 166 The mesh resolution depended on the distance to coastlines and reefs,
 167 bathymetry and bathymetry gradient in order to satisfy SWAN refinement
 168 criterion $h/A \geq a$, where h is the water depth and A is the element area.
 169 The mesh was generated using the Python library seamsh², based on the
 170 the open-source mesh generator GMSH (Geuzaine and Remacle, 2009) and
 171 is composed of approximately 7.7×10^5 elements. The coarsest elements,
 172 far away from the FRT, had a characteristic length size of about 5 km, as
 173 shown in Fig 1 along with the bathymetry of the model domain.

174 2.4 Wave model

175 Waves were modelled using parallel unstructured SWAN (Booij et al., 1999)
 176 on the same mesh as SLIM. This model solves the action balance equation,
 177 which reads (Mei, 1989):

$$\frac{\partial N}{\partial t} + \nabla_{\mathbf{x}} \cdot [(\mathbf{c}_g + \mathbf{u})N] + \frac{\partial}{\partial \theta}[c_\theta N] + \frac{\partial}{\partial \sigma}[c_\sigma N] = \frac{S_{in} + S_{ds} + S_{nl}}{\sigma} \quad (2)$$

178 where $N = E/\sigma$ is the wave action density; θ is the wave propagation direc-
 179 tion; σ is the wave relative frequency; \mathbf{c}_g is the wave group velocity, \mathbf{u} is SLIM
 180 depth-averaged current velocity; c_θ and c_σ are the propagation velocities in
 181 spectral space due to refraction and shifting in frequency due to variations

²<https://pypi.org/project/seamsh/>

182 in depth and currents; and S_{in} , S_{ds} , and S_{nl} respectively represent wave
 183 growth by wind, wave decay and nonlinear transfers of wave energy through
 184 interactions between triplets and quadruplets. Spectra were discretized with
 185 48 direction bins and 50 frequency bins logarithmically distributed from 0.3 to
 186 2 Hz. Exponential wind growth was parameterized using the formulation of
 187 Janssen (1991), while dissipations by whitecapping and bottom dissipations
 188 followed the formulations of Komen et al. (1984) and Madsen et al. (1989)
 189 respectively. Coefficients for exponential wind growth and whitecapping
 190 parameterizations were based on the results of Siadatmousavi et al. (2011).
 191 Finally, wave boundary conditions were derived from WAVEWATCH III (Tol-
 192 man et al., 2009) spectral outputs at buoy locations. Depth-averaged Stokes
 193 drift was also computed by SWAN using the following formula:

$$\mathbf{u}_s = \int_0^{2\pi} \int_0^{+\infty} \frac{\sigma^3}{h \tanh(2kh)} E(\sigma, \theta) (\cos \theta, \sin \theta) d\sigma d\theta \quad (3)$$

194 where k is the norm of the wave vector; h is the water depth; and $E(\sigma, \theta)$ is
 195 the wave energy density.

196 2.5 Coupled model

197 The coupling between SLIM and SWAN is illustrated in Figure 2. The two
 198 models are run consecutively at each time step. First, SLIM computes the
 199 sea surface elevation η and depth-averaged current velocity $\mathbf{u} = (u, v)$.
 200 These quantities are transferred to SWAN to update the model water depth
 201 as well as the second term of equation 2 governing wave energy propagation
 202 in the geographic space. Moreover, in order for the two model to have con-
 203 sistent bottom dissipation parameterizations, SLIM bottom drag coefficient is
 204 transformed into a roughness length z_0 following the methodology of Dietrich
 205 et al. (2011). This roughness length is then converted into Madsen's bottom
 206 dissipation term in SWAN. SWAN then produces the wave-induced force on
 207 current τ_{wave} by computing the wave radiation stress gradient. This quantity
 208 is used to update the value of the surface stress τ_s in equation 1, that now
 209 becomes the sum of wind and wave-induced forces $\tau_s = \tau_{wind} + \tau_{wave}$.

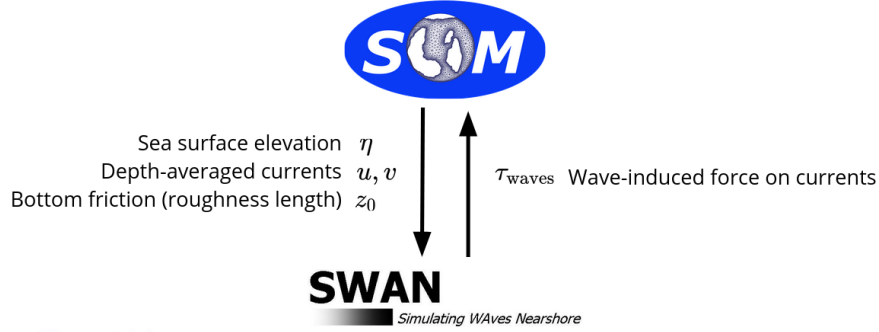


Fig. 2: Schematic illustration of the coupled SLIM+SWAN model.

210 2.6 Comparison of particle trajectories

211 To assess the impact of the wave coupling on the modelled currents during
 212 hurricane Irma, we compared the trajectories of virtual particles driven
 213 by currents produced by SLIM alone and SLIM+SWAN simulations in the
 214 Florida Keys. First, we identified the areas where the differences between
 215 the modelled currents were the largest. Then, we determined the potential
 216 origination regions of particles reaching these areas on the passage of the
 217 hurricane through the Florida Keys using backtracking methods (Dobbelaeere
 218 et al., 2020a). These regions are highlighted by the 4 release regions of Fig.
 219 7. Finally, particles were released from these four regions and advected by
 220 currents produced by the coupled and uncoupled models. At each time step,
 221 the center of mass of the modelled particle clouds were computed. The dis-
 222 tance between these centers of mass was used as a measure of the impact
 223 of the wind-generated wave coupling on the modelled current in the Florida
 224 Keys during hurricane Irma. This comparison was performed with 3 sets
 225 of currents: the currents modelled by uncoupled SLIM (SLIM); the currents
 226 modelled by coupled SLIM+SWAN (SLIM+SWAN); and the SLIM+SWAN
 227 currents with depth-averaged Stokes drift (SLIM+SWAN+Stokes).

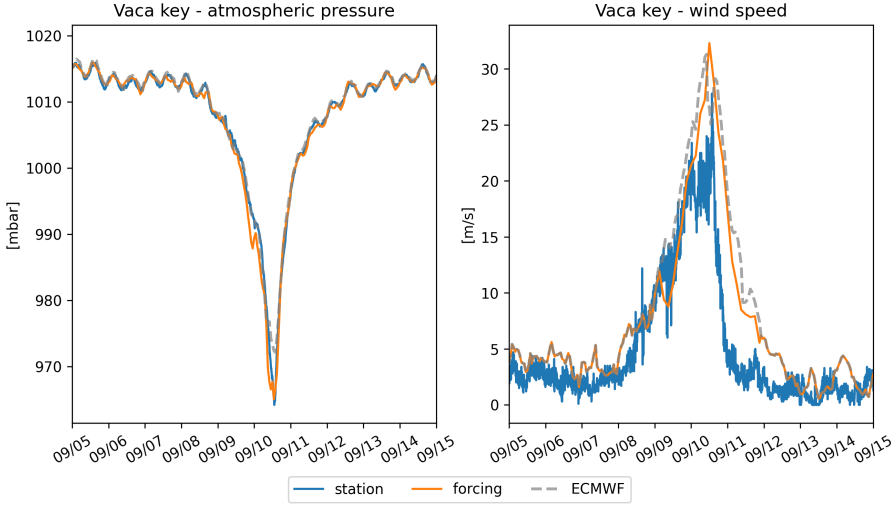


Fig. 3: Comparison of reconstructed wind atmospheric pressure with field measurements and coarser ECMWF ERA-5 profiles during Irma. The generated hybrid atmospheric better capture the observed storm depression while H*wind winds better match the measured peak in wind speed.

228 3 Results

229 3.1 Validation

230 Comparisons of H*Wind wind and hybrid pressure fields with station mea-
 231 surements and ECMWF ERA-5 profiles at Vaca Key station are shown in Fig.
 232 3. The hybrid pressure field shows better agreement with observations than
 233 ERA-5 pressure as it successfully reproduces the storm depression. ERA-5
 234 fields, on the other hand, fail to resolve the low pressure at the core of the
 235 hurricane due to their coarser grid. Both H*Wind and ERA-5 agree well with
 236 observed wind speeds although both data sets tend to slightly overestimate
 237 the width and intensity of the wind peak. However, H*wind profiles show a
 238 better match with the timing of the observed peak, that ERA-5 winds tend
 239 to anticipate. H*wind also exhibits a slightly narrower peak in wind speed,
 240 which better agrees with observations.

241 Hydrodynamic outputs of the coupled wave-current model were validated
 242 against tide gauge and ADCP measurements at the stations highlighted
 243 in Fig. 1. Comparison of modelled and observed sea surface elevation is
 244 shown in Fig. 4. Timing and intensities of the storm surges are successfully

reproduced by the coupled model, the largest model error being an overestimation of 18 cm of the elevation peak at Virginia Key. The fit is especially good at Naples, where both the positive and negative surges are captured by the coupled model with a 5 cm accuracy. This result is of interest as negative surges, although less studied, affect water exchanges between the estuaries and the coastal ocean and disturb the benthic ecosystems (Liu et al., 2020). Modelled 2d currents were validated against depth-averaged ADCP measurements at mooring station C10, C12 and C13 are also shown in Fig. 4. As in (Liu et al., 2020), vector correlation analysis (Kundu, 1976) is performed to compare modelled and observed current velocity vectors. Correlation coefficients (ρ) between simulated and observed depth-averaged currents were 0.84, 0.74 and 0.73 respectively C10, C12 and C13 locations respectively. Average veering angles were computed as well and were below 12° , as in (Liu et al., 2020). However, in our case, no clear overestimation of southward currents was observed during Irma. As expected from a depth-averaged model, the best fit with observations is obtained at the shallowest mooring C10, located on the 25m isobath, with an average veering angle of 6° .

Finally, the modelled wave parameters were validated against observations at the location of the buoys highlighted in Fig. 1, as shown in figure 5. Although the model outputs agree well with observations, a lag in significant wave height is observed for all 4 buoys. Moreover, the peak in significant wave height tends to be underestimated at buoys 41113 and 41114, located on the East Florida Shelf. Other wave parameters were better reproduced by the model on the WFS as well, as illustrated for buoy 42036 in Fig. 5. This good fit on the WFS is not surprising as the parameters used for wind energy input and whitecapping dissipation were based on the calibration performed by (Siadatmousavi et al., 2011) on the Northern Gulf of Mexico. Wind-induced wave growth might therefore be underestimated on the eastern shelf. Consequently, incident wave do not receive enough energy to grow after breaking on the bank boundary, leading to an underestimation of the significant wave height at the location of the buoys. Nonetheless, as this study focused on the wave produced by Irma , that made landfall on the western coasts of Florida, the use of parameterizations calibrated for the Gulf of Mexico seems reasonable.

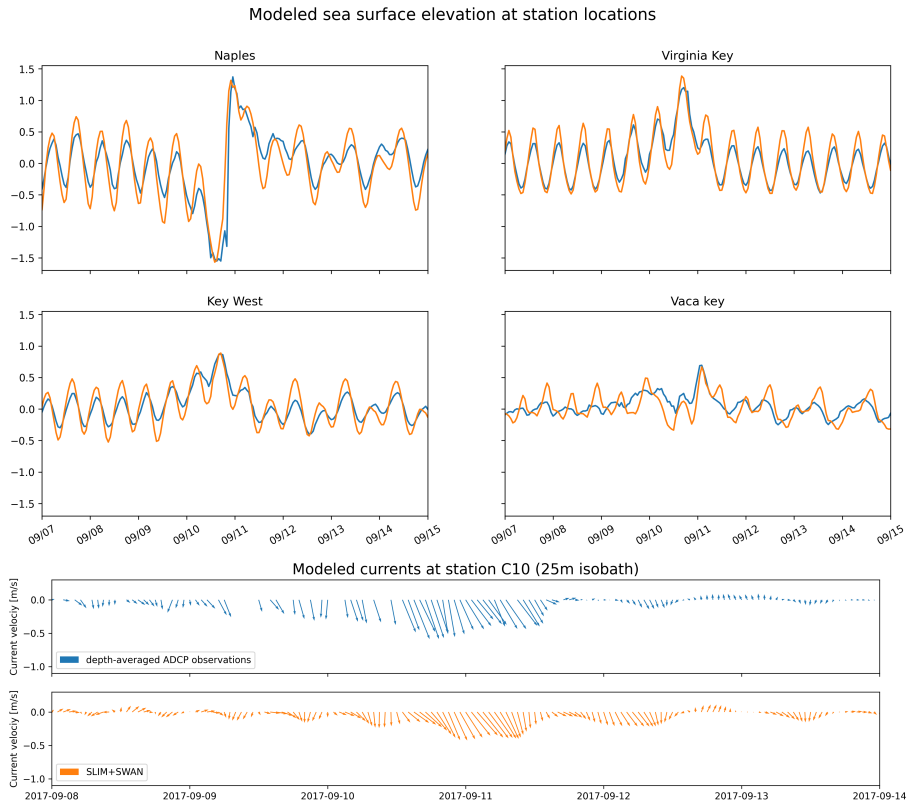


Fig. 4: Comparison of modelled sea surface elevation and current velocity with tide gauge measurements and observed velocity at mooring C10. Timing and intensities of the positive and negative storm surges are well reproduced by the model. Modelled current velocities agree well with observations, with a correlation coefficient of 0.83 and an average veering angle of 6° at mooring C10.

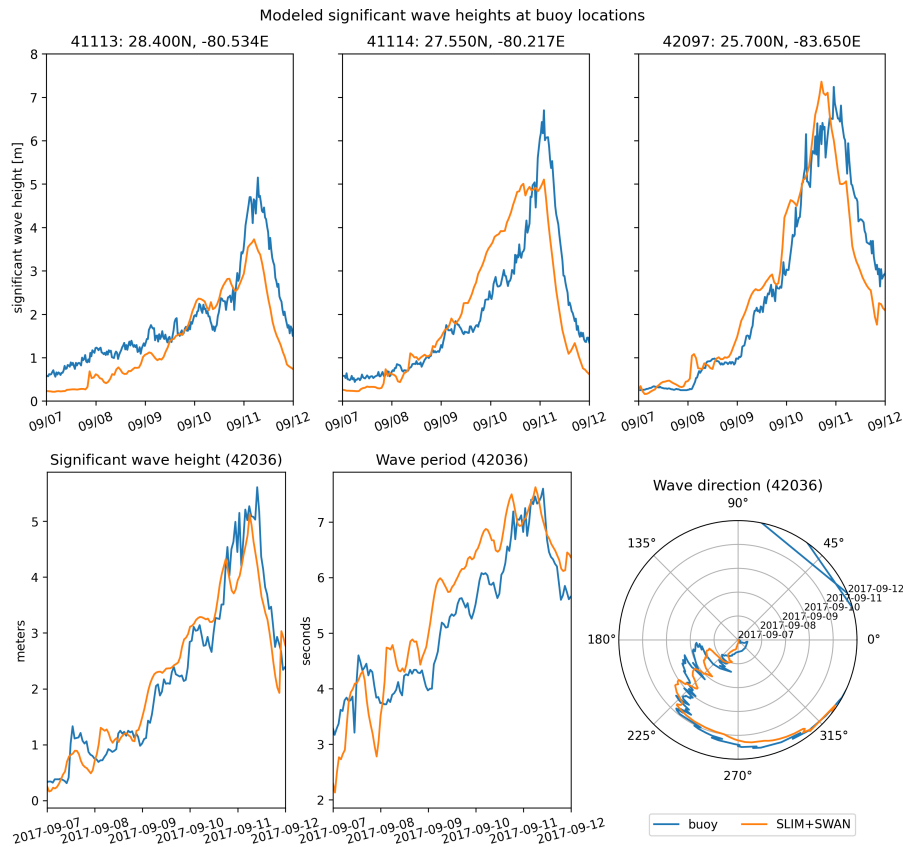


Fig. 5: Comparison of modelled wave parameters with observation at buoys location. Modelled significant wave height agrees well with field measurement. As model parameters were calibrated for the Northern Gulf of Mexico, observations are better reproduced at buoys located on the WFS, as illustrated for buoy 42036

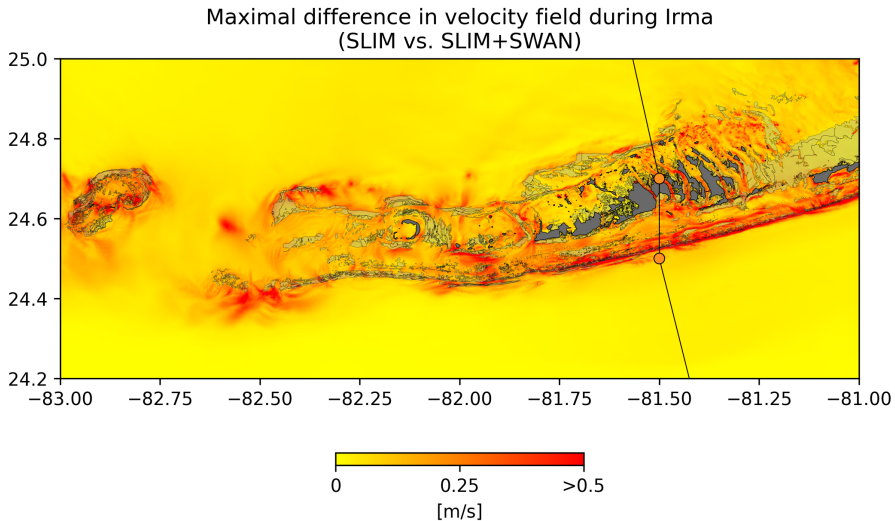


Fig. 6: Maximum of the difference between SLIM and SLIM+SWAN currents speed between 2017-09-07 00:00:00 and 2017-09-13 00:00:00. The difference between the coupled and uncoupled model, which represents the effect of the wave-induced stress, can yield differences of 0.5 m/s in the simulated currents during the passage of the hurricane. SLIM+SWAN currents velocities are larger than the currents modeled by SLIM alone. Islands are highlighted in dark grey and coral reefs in lighter grey

280 3.2 Impact of waves on currents and transport

281 The impact of hurricane-induced wave-current interactions is first evaluated
 282 by computing the norm of the maximal difference in current velocity between
 283 uncoupled SLIM and coupled SLIM+SWAN model runs during the passage
 284 of Irma through the Florida Keys (from 2017-09-07 to 2017-09-13). Figure
 285 6 shows that differences in modelled currents are stronger on the shelf
 286 break and over coral reefs. These results highlight the significant impact
 287 of wave-induced forces, that can yield differences of up to 1 m/s during the
 288 hurricane, with stronger currents being obtained with SLIM+SWAN. This
 289 suggests that neglecting wave-current interactions during Irma would result
 290 in a significant underestimation of transport over reefs.

291 To quantify the impact of these differences in velocity fields on the modelled
 292 trajectories of passive drifters such as coral larvae, we then tracked virtual
 293 particles advected by SLIM, SLIM+SWAN and SLIM+SWAN+Stokes cur-
 294 rents. Comparison of SLIM and SLIM+SWAN+Stokes trajectories are shown

295 in Fig. 7. Differences between the modelled trajectories are negligible before
296 the passage of the hurricanes in the Florida Keys. Then, distance between
297 the centers of mass of the particles abruptly increase to up to tens of kilo-
298 meters as Irma gets through the Keys to finally stabilize after the passage
299 of the hurricane. These results support the assumption that wave-induced
300 transport is negligible compared to advection by Eulerian currents in fair
301 whether conditions. However, ignoring waves in storm conditions could
302 result in significant inaccuracies in modelled trajectories, as illustrated in
303 the case of release region 2 in Fig. 7. Particles advected by the currents
304 of the coupled model tend to remain on the shelf while particles advected
305 by SLIM alone are mostly transported along the shelf break. Although not
306 shown in this paper, comparison of SLIM and SLIM+SWAN trajectories were
307 conducted as well. The evolution of the distance between centers of mass
308 of the particle clouds showed similar trends while yielding smaller values.
309 Modelled maximal depth-averaged Stokes drift reached up to 0.2 m/s during
310 the passage of Irma through the Florida Keys. This suggests that both the
311 impact of wave-induced force on Eulerian currents and Stokes drift should be
312 taken into account while modelling particle transport under storm conditions.

313 4 Discussion and conclusions

- 314 Impact of waves on coral connectivity
- 315 Ability of wave model to correctly capture gradient in significant wave height
316 due to current-waves interactions under tropical cyclones depends on:
- 317 • Spatial (10km → 5km) and spectral (36 dir. → 48 dir.) resolution
318 (Hegermiller et al., 2019)
 - 319 • Directional spreading of incident waves (Villas Bôas et al., 2020)

320 Conflict of Interest Statement

- 321 The authors declare that the research was conducted in the absence of any
322 commercial or financial relationships that could be construed as a potential
323 conflict of interest.

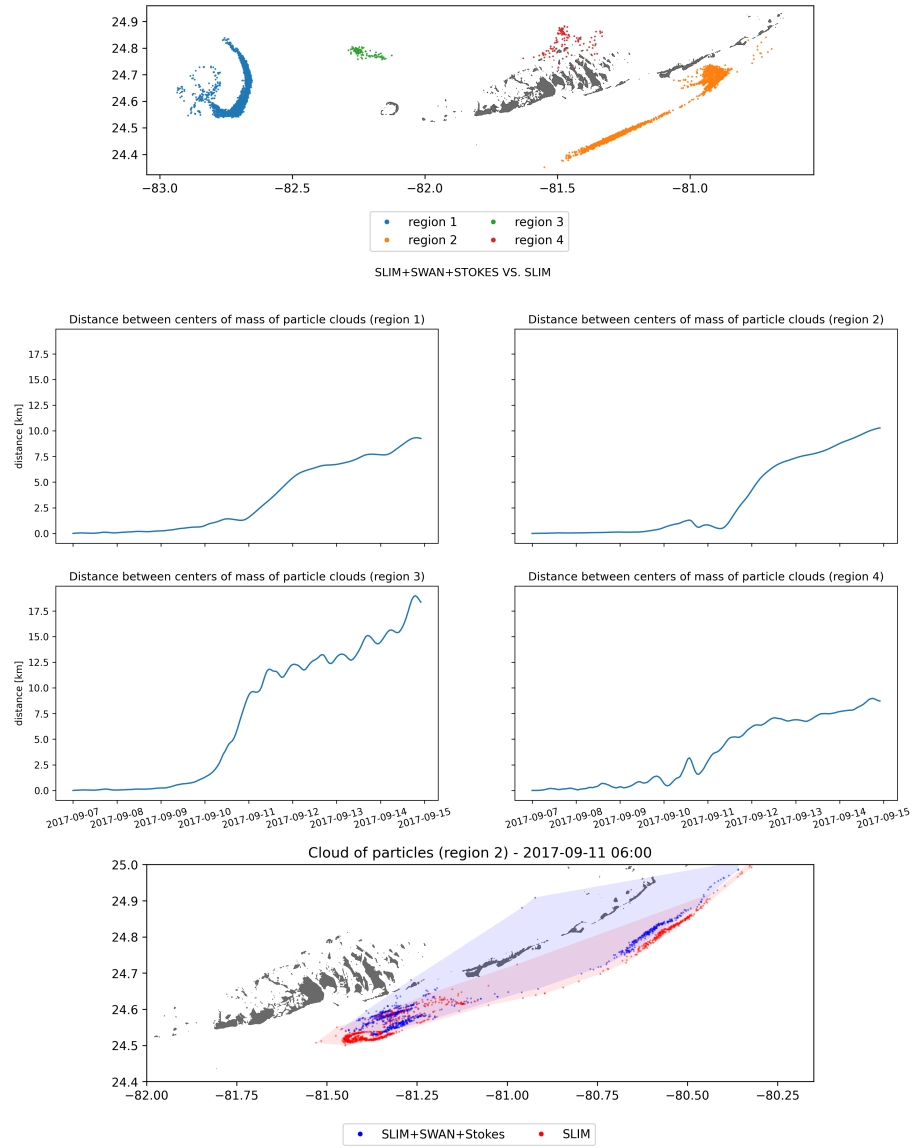


Fig. 7: Comparison of passive drifters trajectories with SLIM+SWAN+Stokes drift vs. SLIM alone. A snapshot of the positions of the particles released from region 2 is shown after the passage of Irma in the Florida Keys. Particles advected by the currents of the coupled model tend to remain on the shelf while particles advected by SLIM alone are mostly transported along the shelf break

324 **Author Contributions**

325 **Funding**

326 **Acknowledgments**

327 Computational resources were provided by the Consortium des Équipements
328 de Calcul Intensif (CÉCI), funded by the F.R.S.-FNRS under Grant No. 2.5020.11.
329 Thomas Dobbelaere is a PhD student supported by the Fund for Research
330 training in Industry and Agriculture (FRIA/FNRS).

331 **Supplementary Material**

332 The Supplementary Material for this article is attached to the submitted
333 document.

334 **References**

- 335 Bever, A. J. and MacWilliams, M. L. (2013). Simulating sediment transport
336 processes in San Pablo Bay using coupled hydrodynamic, wave, and
337 sediment transport models. *Marine Geology*, 345:235–253.
- 338 Booij, N., Ris, R. C., and Holthuijsen, L. H. (1999). A third-generation wave
339 model for coastal regions: 1. Model description and validation. *Journal*
340 *of geophysical research: Oceans*, 104(C4):7649–7666.
- 341 Chassignet, E. P., Hurlbert, H. E., Smedstad, O. M., Halliwell, G. R., Hogan,
342 P. J., Wallcraft, A. J., Baraille, R., and Bleck, R. (2007). The HYCOM
343 (hybrid coordinate ocean model) data assimilative system. *Journal of*
344 *Marine Systems*, 65(1-4):60–83.
- 345 Chen, C., Huang, H., Beardsley, R. C., Liu, H., Xu, Q., and Cowles, G. (2007).
346 A finite volume numerical approach for coastal ocean circulation studies:
347 Comparisons with finite difference models. *Journal of Geophysical*
348 *Research: Oceans*, 112(C3).

- 349 Dietrich, J., Bunya, S., Westerink, J., Ebersole, B., Smith, J., Atkinson,
350 J., Jensen, R., Resio, D., Luettich, R., Dawson, C., et al. (2010). A
351 high-resolution coupled riverine flow, tide, wind, wind wave, and storm
352 surge model for southern Louisiana and Mississippi. part ii: Synoptic
353 description and analysis of hurricanes Katrina and Rita. *Monthly Weather
354 Review*, 138(2):378–404.
- 355 Dietrich, J., Westerink, J., Kennedy, A., Smith, J., Jensen, R., Zijlema, M.,
356 Holthuijsen, L., Dawson, C., Luettich, R., Powell, M., et al. (2011).
357 Hurricane Gustav (2008) waves and storm surge: Hindcast, synoptic
358 analysis, and validation in southern Louisiana. *Monthly Weather Review*,
359 139(8):2488–2522.
- 360 Dobbelaere, T., Muller, E., Gramer, L., Holstein, D., and Hanert, E. (2020a).
361 Report on the potential origin of the SCTLD in the Florida Reef Tract.
362 Available online at: [https://floridadep.gov/rcp/coral/documents/
363 report-potential-origin-sctld-florida-reef-tract](https://floridadep.gov/rcp/coral/documents/report-potential-origin-sctld-florida-reef-tract).
- 364 Dobbelaere, T., Muller, E. M., Gramer, L. J., Holstein, D. M., and Hanert, E.
365 (2020b). Coupled epidemi-hydrodynamic modeling to understand the
366 spread of a deadly coral disease in Florida. *Frontiers in Marine Science*,
367 7:1016.
- 368 Donelan, M., Haus, B., Reul, N., Plant, W., Stiassnie, M., Gruber, H., Brown,
369 O., and Saltzman, E. (2004). On the limiting aerodynamic roughness of
370 the ocean in very strong winds. *Geophysical Research Letters*, 31(18).
- 371 Figueiredo, J., Baird, A. H., and Connolly, S. R. (2013). Synthesizing larval
372 competence dynamics and reef-scale retention reveals a high potential
373 for self-recruitment in corals. *Ecology*, 94(3):650–659.
- 374 Frys, C., Saint-Amand, A., Le Hénaff, M., Figueiredo, J., Kuba, A., Walker, B.,
375 Lambrechts, J., Vallaeyns, V., Vincent, D., and Hanert, E. (2020). Fine-
376 scale coral connectivity pathways in the Florida Reef Tract: implications
377 for conservation and restoration. *Frontiers in Marine Science*, 7:312.
- 378 Garcia-Pineda, O., Androulidakis, Y., Le Hénaff, M., Kourafalou, V., Hole,
379 L. R., Kang, H., Staples, G., Ramirez, E., and DiPinto, L. (2020). Mea-
380 suring oil residence time with GPS-drifters, satellites, and Unmanned
381 Aerial Systems (UAS). *Marine pollution bulletin*, 150:110644.

- 382 Geuzaine, C. and Remacle, J.-F. (2009). Gmsh: A 3-d finite element mesh
383 generator with built-in pre-and post-processing facilities. *International*
384 *journal for numerical methods in engineering*, 79(11):1309–1331.
- 385 Harper, B., Kepert, J., and Ginger, J. (2010). *Guidelines for converting*
386 *between various wind averaging periods in tropical cyclone conditions*.
387 Citeseer.
- 388 Hegermiller, C. A., Warner, J. C., Olabarrieta, M., and Sherwood, C. R.
389 (2019). Wave–current interaction between Hurricane Matthew wave
390 fields and the Gulf Stream. *Journal of Physical Oceanography*,
391 49(11):2883–2900.
- 392 Hoffmeister, J. and Multer, H. (1968). Geology and origin of the Florida Keys.
393 *Geological Society of America Bulletin*, 79(11):1487–1502.
- 394 Holthuijsen, L. H., Powell, M. D., and Pietrzak, J. D. (2012). Wind and waves
395 in extreme hurricanes. *Journal of Geophysical Research: Oceans*,
396 117(C9).
- 397 Janssen, P. A. (1991). Quasi-linear theory of wind-wave generation applied
398 to wave forecasting. *Journal of physical oceanography*, 21(11):1631–
399 1642.
- 400 Johns, W. E. and Schott, F. (1987). Meandering and transport variations
401 of the Florida Current. *Journal of physical oceanography*, 17(8):1128–
402 1147.
- 403 Knaff, J. A., Sampson, C. R., and Musgrave, K. D. (2018). Statistical tropi-
404 cal cyclone wind radii prediction using climatology and persistence:
405 Updates for the western North Pacific. *Weather and Forecasting*,
406 33(4):1093–1098.
- 407 Knutson, T. R., McBride, J. L., Chan, J., Emanuel, K., Holland, G., Landsea,
408 C., Held, I., Kossin, J. P., Srivastava, A., and Sugi, M. (2010). Tropical
409 cyclones and climate change. *Nature geoscience*, 3(3):157–163.
- 410 Komen, G., Hasselmann, S., and Hasselmann, K. (1984). On the exis-
411 tence of a fully developed wind-sea spectrum. *Journal of physical*
412 *oceanography*, 14(8):1271–1285.

- 413 Kourafalou, V. H. and Kang, H. (2012). Florida Current meandering and
414 evolution of cyclonic eddies along the Florida Keys Reef Tract: Are they
415 interconnected? *Journal of Geophysical Research: Oceans*, 117(C5).
- 416 Kundu, P. K. (1976). Ekman veering observed near the ocean bottom.
417 *Journal of Physical Oceanography*, 6(2):238–242.
- 418 Landsea, C. W. and Franklin, J. L. (2013). Atlantic hurricane database un-
419 certainty and presentation of a new database format. *Monthly Weather
420 Review*, 141(10):3576–3592.
- 421 Lee, T. N., Leaman, K., Williams, E., Berger, T., and Atkinson, L. (1995).
422 Florida Current meanders and gyre formation in the southern Straits
423 of Florida. *Journal of Geophysical Research: Oceans*, 100(C5):8607–
424 8620.
- 425 Lee, T. N. and Mayer, D. A. (1977). Low-frequency current variability and
426 spin-off eddies along the shelf off southeast Florida. *Collected Reprints*,
427 1(1):344.
- 428 Lee, T. N. and Smith, N. (2002). Volume transport variability through the
429 Florida Keys tidal channels. *Continental Shelf Research*, 22(9):1361–
430 1377.
- 431 Lee, T. N. and Williams, E. (1988). Wind-forced transport fluctuations of the
432 Florida Current. *Journal of Physical Oceanography*, 18(7):937–946.
- 433 Li, Z. and Johns, B. (1998). A three-dimensional numerical model of surface
434 waves in the surf zone and longshore current generation over a plane
435 beach. *Estuarine, Coastal and Shelf Science*, 47(4):395–413.
- 436 Lidz, B. H. and Shinn, E. A. (1991). Paleoshorelines, reefs, and a rising sea:
437 South florida, usa. *Journal of Coastal Research*, pages 203–229.
- 438 Lin, N. and Chavas, D. (2012). On hurricane parametric wind and appli-
439 cations in storm surge modeling. *Journal of Geophysical Research:
440 Atmospheres*, 117(D9).
- 441 Liu, Y. and Weisberg, R. H. (2012). Seasonal variability on the West Florida
442 shelf. *Progress in Oceanography*, 104:80–98.

- 443 Liu, Y., Weisberg, R. H., and Zheng, L. (2020). Impacts of hurricane Irma
444 on the circulation and transport in Florida Bay and the Charlotte Harbor
445 estuary. *Estuaries and Coasts*, 43(5):1194–1216.
- 446 Liubartseva, S., Coppini, G., Lecci, R., and Clementi, E. (2018). Tracking
447 plastics in the Mediterranean: 2D Lagrangian model. *Marine pollution
448 bulletin*, 129(1):151–162.
- 449 Longuet-Higgins, M. S. (1970). Longshore currents generated by obliquely
450 incident sea waves. *Journal of geophysical research*, 75(33):6778–
451 6789.
- 452 Longuet-Higgins, M. S. and Stewart, R. (1964). Radiation stresses in water
453 waves; a physical discussion, with applications. In *Deep sea research
454 and oceanographic abstracts*, volume 11, pages 529–562. Elsevier.
- 455 Madsen, O. S., Poon, Y.-K., and Gruber, H. C. (1989). Spectral wave
456 attenuation by bottom friction: Theory. In *Coastal Engineering 1988*,
457 pages 492–504.
- 458 Malmstadt, J., Scheitlin, K., and Elsner, J. (2009). Florida hurricanes and
459 damage costs. *southeastern geographer*, 49(2):108–131.
- 460 Marsooli, R., Lin, N., Emanuel, K., and Feng, K. (2019). Climate change
461 exacerbates hurricane flood hazards along US Atlantic and Gulf Coasts
462 in spatially varying patterns. *Nature communications*, 10(1):1–9.
- 463 Mei, C. C. (1989). *The applied dynamics of ocean surface waves*, volume 1.
464 World scientific.
- 465 Moon, I.-J., Ginis, I., Hara, T., and Thomas, B. (2007). A physics-based
466 parameterization of air–sea momentum flux at high wind speeds and
467 its impact on hurricane intensity predictions. *Monthly weather review*,
468 135(8):2869–2878.
- 469 Pinelli, J.-P., Roueche, D., Kijewski-Correa, T., Plaz, F., Prevatt, D., Zisis,
470 I., Elawady, A., Haan, F., Pei, S., Gurley, K., et al. (2018). Overview
471 of damage observed in regional construction during the passage of
472 Hurricane Irma over the State of Florida. In *Forensic Engineering 2018:
473 Forging Forensic Frontiers*, pages 1028–1038. American Society of
474 Civil Engineers Reston, VA.

- 475 Powell, M. D., Houston, S. H., Amat, L. R., and Morisseau-Leroy, N. (1998).
476 The HRD real-time hurricane wind analysis system. *Journal of Wind*
477 *Engineering and Industrial Aerodynamics*, 77:53–64.
- 478 Powell, M. D., Vickery, P. J., and Reinhold, T. A. (2003). Reduced drag coeffi-
479 cient for high wind speeds in tropical cyclones. *Nature*, 422(6929):279–
480 283.
- 481 Schott, F. A., Lee, T. N., and Zantopp, R. (1988). Variability of structure and
482 transport of the Florida Current in the period range of days to seasonal.
483 *Journal of Physical Oceanography*, 18(9):1209–1230.
- 484 Shinn, E. A. (1988). The geology of the Florida Keys. *Oceanus*, 31(1):46–53.
- 485 Siadatmousavi, S. M., Jose, F., and Stone, G. (2011). Evaluation of two WAM
486 white capping parameterizations using parallel unstructured SWAN
487 with application to the Northern Gulf of Mexico, USA. *Applied Ocean*
488 *Research*, 33(1):23–30.
- 489 Sikirić, M. D., Roland, A., Janeković, I., Tomazić, I., and Kuzmić, M. (2013).
490 Coupling of the Regional Ocean Modeling System (roms) and Wind
491 Wave Model. *Ocean Modelling*, 72:59–73.
- 492 Smith, N. P. (1982). Response of Florida Atlantic shelf waters to hurricane
493 David. *Journal of Geophysical Research: Oceans*, 87(C3):2007–2016.
- 494 Tolman, H. L. et al. (2009). User manual and system documentation of
495 WAVEWATCH III TM version 3.14. *Technical note, MMAB Contribution*,
496 276:220.
- 497 Van Den Bremer, T. and Breivik, Ø. (2018). Stokes drift. *Philosophical Trans-*
498 *actions of the Royal Society A: Mathematical, Physical and Engineering*
499 *Sciences*, 376(2111):20170104.
- 500 Villas Bôas, A. B., Cornuelle, B. D., Mazloff, M. R., Gille, S. T., and Arduin,
501 F. (2020). Wave–current interactions at meso-and submesoscales:
502 Insights from idealized numerical simulations. *Journal of Physical*
503 *Oceanography*, 50(12):3483–3500.
- 504 Weisberg, R., Liu, Y., and Mayer, D. (2009). Mean circulation on the west
505 Florida continental shelf observed with long-term moorings. *Geophys.*
506 *Res. Lett*, 36:L19610.

- 507 Weisberg, R. H. and Zheng, L. (2006). Hurricane storm surge simulations
508 for Tampa Bay. *Estuaries and Coasts*, 29(6):899–913.
- 509 Wu, L., Chen, C., Guo, P., Shi, M., Qi, J., and Ge, J. (2011). A FVCOM-
510 based unstructured grid wave, current, sediment transport model, I.
511 Model description and validation. *Journal of Ocean University of China*,
512 10(1):1–8.
- 513 Xian, S., Feng, K., Lin, N., Marsooli, R., Chavas, D., Chen, J., and Hatzikyri-
514 akou, A. (2018). Brief communication: Rapid assessment of damaged
515 residential buildings in the Florida Keys after Hurricane Irma. *Natural
516 Hazards and Earth System Sciences*, 18(7):2041–2045.
- 517 Zhang, C., Durgan, S. D., and Lagomasino, D. (2019). Modeling risk of man-
518 groves to tropical cyclones: A case study of Hurricane Irma. *Estuarine,
519 Coastal and Shelf Science*, 224:108–116.